Spectral Classification of Targets Below a Random Rough Air–Soil Interface

Arnold D. Kim and Chrysoula Tsogka

***Abstract*— Motivated by the use of unmanned aerial vehicles (UAVs) for buried landmine detection, we consider the spectral classification of dispersive point targets below a rough air–soil interface. The target location can be estimated using a previously developed method for ground-penetrating synthetic aperture radar involving principal component analysis for ground bounce removal and Kirchhoff migration. For the classification problem, we use the approximate location determined from this imaging method to recover the spectral characteristics of the target over the system bandwidth. For the dispersive point target we use here, this spectrum corresponds to its radar cross section (RCS). For a more general target, this recovered spectrum is a proxy for the frequency dependence of the RCS averaged over angles spanning the synthetic aperture. The recovered spectrum is noisy and exhibits an overall scaling error due to modeling errors. Nonetheless, by smoothing and normalizing this recovered spectrum, we compare it with a library of precomputed normalized spectra in a simple multiclass classification scheme. Numerical simulations in two dimensions validate this method and show that this spectral estimation method is effective for target classification.**

***Index Terms*— Classification, dispersive targets, ground-penetrating synthetic aperture radar, Kirchhoff migration (KM), radar cross section (RCS) spectrum.**

I. Introduction

UNMANNED aerial vehicles (UAVs) equipped with ground-penetrating radar provide a means for imaging subsurface targets, such as buried landmines, while keeping a safe distance from the inspected area [1], [2]. A key feature of UAV-based ground-penetrating synthetic aperture radar is that the flight paths can be relatively low in elevation and short in distance, thereby allowing for site-specific imaging. Several challenges need to be addressed, such as limited apertures, soil heterogeneity, soil surface roughness, and measurement noise. The occurrence of false positives, where benign objects appear as targets in images, is especially challenging since addressing this problem requires some sort of quantitative imaging method to distinguish true targets from false positives. We present here a proof-of-concept study that 1) recovers spectral information about the target located beneath a rough air–soil interface and 2) uses that spectral information to classify it.

Received 30 October 2024; revised 14 December 2024; accepted 19 December 2024. Date of publication 23 December 2024; date of current version 8 January 2025. This work was supported by AFOSR under Grant FA9550-24-1-0196. The work of Arnold D. Kim was supported by NSF under Grant DMS-1840265. *(Corresponding author: Chrysoula Tsogka.)*

The authors are with the Department of Applied Mathematics, University of California at Merced, Merced, CA 95343 USA (e-mail: adkim@ucmerced.edu; ctsogka@ucmerced.edu).

Digital Object Identifier 10.1109/LGRS.2024.3521342

For a general target, its far-field scattering behavior is given by the scattering amplitude [3]. This scattering amplitude depends on the target size, shape, and material properties. In general, it is a function of the incident direction $\hat{\boldsymbol{\imath}}$, the scattered direction $\hat{\boldsymbol{o}}$, and frequency f. For monostatic synthetic aperture imaging systems, we measure only backscattering, so measurements are limited to $\hat{\boldsymbol{o}} = -\hat{\boldsymbol{\imath}}$. Moreover, the synthetic aperture effectively subtends only a relatively small range of directions. Therefore, synthetic aperture imaging measurements are extremely limited with respect to the directional dependence of the scattering amplitude. In contrast, the frequency dependence which is limited only by the system bandwidth may be more useful.

We have recently introduced a dispersive point target model that explicitly incorporates a frequency-dependent scattering amplitude with an isotropic angular dependence [4]. This simplified model may be related to the average of the scattering amplitude over the directions sampled over a synthetic aperture. This averaged interpretation applies to a sphere or a nearly spherical target, but may not be correct for a general target. We expect the proposed dispersive point target model to work when the size of the target is of the same order or smaller than the resolution of the imaging system that can be analyzed using an approach as in [5]. We use this model here to investigate the potential for spectral classification of subsurface targets.

The remainder of this letter is as follows. In Section II, we describe the problem and specify the set of measurements. We briefly review the imaging method we have developed that identifies and locates targets below an unknown rough air–soil interface in Section III. In Section IV, we give the method we use for recovering the radar cross section (RCS) spectrum of a dispersive point target. We then show simulation results in Section V that demonstrate the potential for multiclass classification using this recovered RCS spectrum. We give our conclusions in Section VI.

II. Problem Description

A sketch of the physical problem is illustrated in Fig. 1. As a UAV travels along its flight path, it emits a multifrequency signal at frequencies f_m for $m = 1, \ldots, M$, that propagates downward. Part of this signal is reflected by the air–soil interface (ground bounce) and the other part penetrates the soil and scatters off of the subsurface target. The receiver on the UAV measures both the ground bounce and scattered signals. This procedure is repeated at various points $\boldsymbol{x}_n$ for

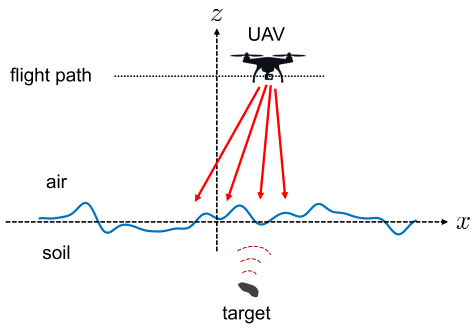

Fig. 1. Sketch of the physical problem.

$n = 1, \ldots, N$ along the flight path making up the synthetic aperture. The measurements are collected as the matrix $D \in \mathbb{C}^{M\times N}$ whose entry d_{mn} is the signal measured at frequency f_m and spatial location $\boldsymbol{x}_n$. An integral equation expression for d_{mn} is given in [6, Sec. 4].

For the simulation results presented here, we have used $M = 41$ frequencies uniformly sampling the band from 3.1 to 5.1 GHz. In addition, we have used $N = 35$ spatial measurements uniformly sampling a linear synthetic aperture of length $a = 102$ cm. The elevation of the platform is set to 75 cm above the mean height of the air–soil interface. Following Daniels [7], we use $\epsilon_r = 9$ as relative dielectric constant for the soil.

We model a rough air–soil interface using a mean-zero Gaussian correlated random function parameterized by its correlation length, l, and its root-mean-square (rms) height, h_{rms} [8]. In the simulations, we set $l = 8$ cm and $h_{\text{rms}} = 0.2$ cm. We have shown previously that a rough air–soil interface with these parameters over this frequency band exhibits enhanced backscattering [6]. The occurrence of enhanced backscattering indicates that the rough air–soil interface causes significant multiple scattering. We have recently applied the method of fundamental solutions (MFS) to solve boundary value problems with rough air–soil interfaces [9]. This method is closely related to boundary integral equation formulations of the problem [6], [8] that are typically used, but is easier to implement and accurately accounts for multiple scattering. We have used this MFS implementation for the simulation results that follow.

III. Imaging

We have recently developed a method to identify and locate targets below an unknown rough air–soil interface [6]. We briefly summarize this method and show some results that characterize its effectiveness.

The main challenge with subsurface imaging is that ground bounce signals dominate and obscure signals scattered by the targets. To remove those ground bounce signals from measurements, we apply PCA as follows. First, we compute the singular value decomposition, $D = U\Sigma V^{\text{H}}$, where $[\cdot]^{\text{H}}$ denotes the Hermitian or conjugate transpose. We then set a truncation level, denoted by j^*, and compute $\tilde{D} = D - \sigma_1 \mathbf{u}_1 \mathbf{v}_1^{\text{H}} - \cdots - \sigma_{j^*} \mathbf{u}_{j^*} \mathbf{v}_{j^*}^{\text{H}}$.

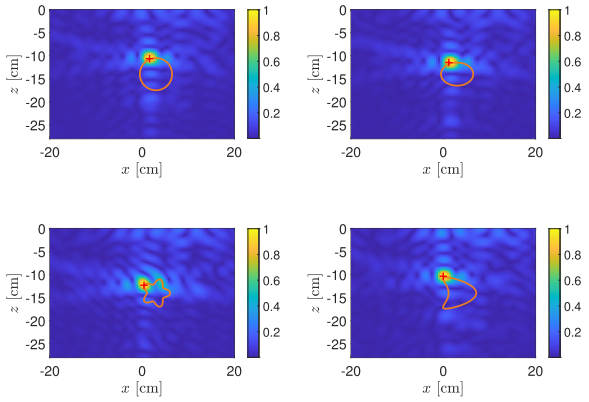

Fig. 2. KM imaging results for different shaped targets plotted as solid orange curves. All targets are situated below a random rough air–soil interface with correlation length $l = 8$ cm and rms height $h_{\text{rms}} = 0.2$ cm. PCA was used to remove ground bounce signals using $j^* = 2$. The relative dielectric constant for all targets was set to $\epsilon_r = 2.3$. The red "+" symbols in each of the plots indicate where the imaging function attains its maximum absolute value.

Using $\tilde{D}$, we evaluate the Kirchhoff migration (KM) imaging function

$$I^{\text{KM}}(\boldsymbol{y}) = \sum_{m=1}^{M}\sum_{n=1}^{N} \tilde{d}_{\text{mn}} a^*_{\text{mn}}(\boldsymbol{y}) \tag{1}$$

on position $\boldsymbol{y}$ in the imaging region. Here, $\tilde{d}_{\text{mn}}$ is the (m, n)th entry of $\tilde{D}$ and $a^*_{\text{mn}}(\boldsymbol{y})$ is the complex conjugate of the signal at frequency f_m measured at spatial location $\boldsymbol{x}_n$ scattered by a nondispersive point target located at $\boldsymbol{y}$ below the flat air–soil interface $z = 0$. An expression for $a_{\text{mn}}(\boldsymbol{y})$ is given in [6, Sec. 6.1].

The appropriate truncation j^* is not theoretically known. Empirically, we find that when j^* is too small, the resulting image produces large artifacts near the interface, but at some truncation, those artifacts are gone and the resulting image concentrates on the actual target. For the simulations shown here, we have used $j^* = 2$.

Fig. 2 shows plots of the absolute value of I^{KM} given in (1) for several different target shapes whose boundaries are plotted as solid orange curves in each of the figures. All of these targets have a characteristic size that is approximately 7 cm, which is comparable to the central wavelength. The relative dielectric constant for all targets is $\epsilon_r = 2.3$. Even though the different targets have significantly different shapes, the resulting KM images only exhibit a single peak at a representative point. The imaging method is unable to do more because of the limited spatial resolution of the imaging setup.

IV. Recovering the RCS Spectrum

The imaging method provides an approximate spatial location for subsurface targets, but no other information. Hence, it cannot be used to characterize differences between any two targets, thereby creating opportunities for false positives. Moreover, measurements over the limited aperture do not capture much variation in the directional dependence of the scattering amplitude. For these reasons, we consider the dispersive point target model [4] to recover characterizing spectral information about subsurface targets that can mitigate false positives. A dispersive point target scatters isotropically from

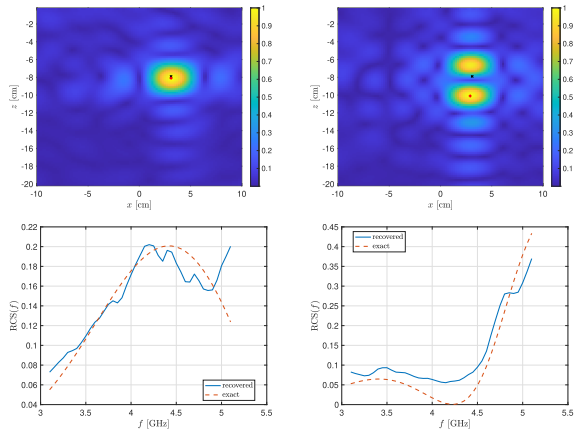

Fig. 3. Results for dispersive point targets situated below a random rough air–soil interface with $l = 8$ cm and $h_{\text{rms}} = 0.2$ cm. Reflectivities computed from two circular disk targets with relative dielectric constant, $\epsilon_r = 2.3$, and radius 1.5 cm (left column) and 2.0 cm (right column) are considered. (Top row) KM images with the true target location plotted as a black "×" and the estimated location as a red "+". (Bottom row) Recovered RCS spectrum after smoothing and normalization (solid curve) compared to the exact normalized RCS spectrum (dashed curve).

the location $\boldsymbol{y}_0$ and has an explicit frequency dependence which we denote by $\varrho(f)$ and call the reflectivity. The RCS of a dispersive point target is given by $\text{RCS}(f) = 4\pi|\varrho(f)|^2$. For a more general target shape, this frequency-dependent quantity may be interpreted as the average over the angles spanned by the aperture of the frequency and angular-dependent RCS.

We seek to recover the RCS spectrum of a dispersive point target from the measurements $\tilde{D}$. In the results shown in Fig. 2, we see that we can easily recover an estimate for the target location, which we denote here by $\hat{\boldsymbol{y}}_0$, by determining where the absolute value of the KM image attains its maximum (plotted as a red "+" symbol in each of the images). With $\hat{\boldsymbol{y}}_0$ determined, we estimate the RCS spectrum through the evaluation of

$$\text{RCS}(f_m) = 4\pi\left(\frac{1}{N}\sum_{n=1}^{N}\frac{|\tilde{d}_{\text{mn}}a^*_{\text{mn}}(\hat{\boldsymbol{y}}_0)|}{|a_{\text{mn}}(\hat{\boldsymbol{y}}_0)|^2}\right)^2. \tag{2}$$

For a flat air–soil interface, $\tilde{d}_{\text{mn}} \approx \varrho(f_m)a_{\text{mn}}(\boldsymbol{y}_0) + \eta_{\text{mn}}$ with η_{mn} denoting the error from measurement noise, modeling error, and so on. The ordinary least-squares solution to this problem is $\hat{\varrho}(f_m) = d_{\text{mn}}a^*_{\text{mn}}(\boldsymbol{y}_0)/|a_{\text{mn}}(\boldsymbol{y}_0)|^2$. We further reduce the effect due to noise by averaging these results over $n = 1, \ldots, N$. By multiplying 4π to the absolute value squared of that average, we obtain (2).

For a nearly flat air–soil interface, (2) gives a very accurate estimate. It is less accurate for rough air–soil interface due to modeling error manifested as a random phase perturbations. Those phase perturbations produce spurious oscillations in the recovered RCS spectrum. Moreover, its magnitude will not be accurate because this estimation does not accurately account for the total power of the scattered signals. After applying a smoothing algorithm to help reduce the noisy estimate, we introduce the M-vector, $\mathbf{v} = (\text{RCS}(f_1), \ldots, \text{RCS}(f_M))$, and consider the normalization $\hat{\mathbf{v}} = \mathbf{v}/\|\mathbf{v}\|$.

Results for two dispersive point targets situated below a random rough air–soil interface with $l = 8$ cm and $h_{\text{rms}} = 0.2$ cm are shown in Fig. 3. We have used the scattering

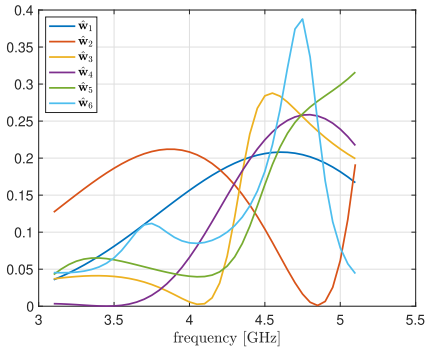

Fig. 4. Set of normalized RCS spectra used as classifiers, $\hat{\mathbf{w}}_i$ for $i = 1, \ldots, 6$.

amplitude for circular disk targets with relative dielectric constant $\epsilon_r = 2.3$ to compute $\varrho(f)$. The left column of Fig. 3 show results for radius 1.5 cm and the right column shows results for radius 2.0 cm. The resulting KM images are shown in the top row of Fig. 3 for the two cases look quite different and we note that for the bigger disk, two peaks are obtained. In each image, the true target location is indicated with a black "×" and the estimated one with a red "+." The bottom row in Fig. 3 shows the comparison of the estimated, smoothed, and normalized RCS spectrum with the exact one that has also been normalized. These results exhibit an overall qualitative agreement with the exact RCS spectra but also exhibit spurious oscillations. We remark, however, that the two RCS spectra look very different from one another suggesting the estimated RCS spectrum may be used for classification.

V. Spectral Classification

For multiclass classification of a recovered RCS spectrum, we consider the matrix W whose columns $\hat{\mathbf{w}}_j$ for $j = 1, \ldots, 6$ are M-vectors that are the exact RCS spectra for six different reflectivities computed from circular disk targets. Columns 1–3 are computed from circular disks all with radius 1.5 cm and with relative dielectric constants, $\epsilon_r = 2$, 3.5, and 5, respectively. Columns 4–6 are computed from circular disks all with radius 2.5 cm, and with $\epsilon_r = 2$, 3.5, and 5, respectively. All of these RCS spectra are normalized by their respective norms. We show plots of these six normalized RCS spectra in Fig. 4.

Suppose we recover an estimated RCS spectrum, smooth it, and normalize it using the method described above to obtain the vector $\hat{\mathbf{v}}$. To perform a multiclass classification for this RCS spectrum, we compute $\mathbf{c} = W^T\hat{\mathbf{v}}$. Since all vectors involved are normalized, the entries of $\mathbf{c}$ satisfy $0 \le c_j \le 1$ for $j = 1, \ldots, 6$. Classification is done by determining which element of the 6-D vector $\mathbf{c}$ is largest. That element corresponds to the column of W to which the recovered RCS spectrum is classified.

To test the effectiveness of this classification method, we simulate measurements for dispersive point targets whose reflectivities are computed from 36 different circular disk targets whose radii are either 1.5 or 2.5 cm and whose values of ϵ_r are a random perturbation of $\epsilon_r = 2$, 3.5, or 5. To those simulated measurements, we have added noise so that SNR $\approx$ 25 dB. In [4], we have shown that the estimated target

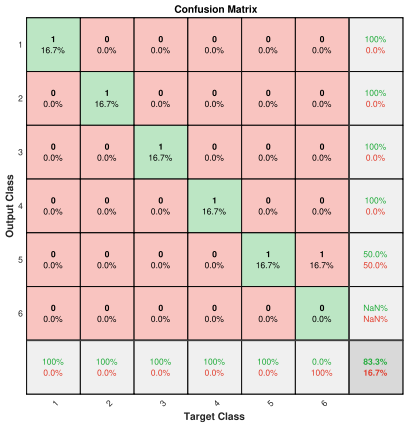

Fig. 5. Confusion matrix for the classification of 36 different dispersive point targets computed from circular disks whose radii are either 1.5 or 2.5 cm and the values of ϵ_r are random perturbation from either $\epsilon_r = 2$, 3.5, or 5.

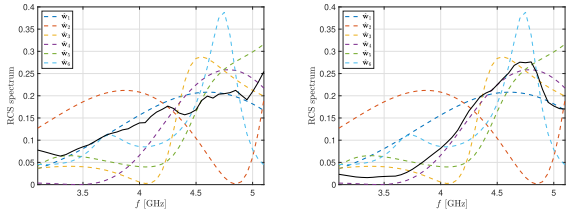

Fig. 6. Examples of recovered RCS spectra (solid black curves) compared with classifiers. The left plot shows a case that is classified with $\hat{\mathbf{w}}_1$, and the right plot shows a case that is classified to $\hat{\mathbf{w}}_4$.

location using (1) is shifted slightly from the exact location, but the recovered RCS spectrum is accurate. We assume that the estimated target location is exact so that $\hat{\boldsymbol{y}}_0 = \boldsymbol{y}_0$ and evaluate (2). We smooth and normalize that result to compute $\hat{\mathbf{v}}$ and then perform the classification method described above.

We show the confusion matrix in Fig. 5 resulting from these simulations. These results show that targets are classified into the class corresponding to the correct value of the radius. With respect to ϵ_r, all targets are correctly classified except for those in class 6 which are classified as belonging to class 5.

In Fig. 6, we show individual examples of recovered RCS spectra that have been smoothed and normalized (solid black curves) compared with the classifiers (dashed curves). Even though those recovered RCS spectra are quite noisy, they exhibit enough behavioral characteristics to allow for successful classification. The classification we have used here only involves inner products of the recovered RCS spectrum with the classifiers. There are much more sophisticated multiclass classification methods available. Nonetheless, the results from this simple classification method suggest that the RCS spectra recovered using (2) may be potentially useful in practice.

As the number of classes increases, the vectors $\hat{\mathbf{w}}_i$ may become more and more aligned with each other in which case classification will most likely fail. We begin to see this happening in Fig. 5 (right) where targets from class 6 were classified as class 5. For this reason, it is important to carefully select a few number of distinct targets (e.g., types of mines) to use for classifiers. As long as these classifiers are sufficiently incoherent (i.e., $|\hat{\mathbf{w}}_i^{\mathrm{H}}\hat{\mathbf{w}}_j| \ll 1$ for $i \neq j$), classification should be possible. Then, given data corresponding to a target in the field one could check if these data belong to one of the classified targets or not. This approach has limitations and classification errors may happen. Increasing the bandwidth or using lower frequencies may help.

VI. Conclusion

We have developed a method for spectrally classifying dispersive point targets below an unknown rough air–soil interface from ground-penetrating synthetic aperture radar measurements. The method requires three steps. The first step relies on PCA to approximately remove ground bounce signals from measurements. The second step employs KM using a model with a flat air–soil interface, that is, evaluation of (1) to locate targets in some prescribed imaging region. Because of inherent limitations in synthetic aperture measurements, the images produced only identify a single point for a target. Upon using that point as an approximate location for a target, the third step involves the evaluation of (2) to recover an estimate of the RCS spectrum. This RCS spectrum will have inherent errors in its magnitude because power is not accurately taken into account when applying PCA or when using the flat air–soil interface model. Nonetheless, we have shown here that this recovered RCS spectrum can be successfully used in a multiclass classification method.

Although the simulation results we present here are limited to 2-D problems with a single dispersive point target, nothing in the methods we have introduced is limited by these assumptions. PCA for ground bounce removal, KM for imaging, and the evaluation of (2) to estimate the RCS spectrum can all be easily extended to 3-D problems for more general targets. For these reasons, we believe that the results shown here serve as a proof-of-concept and indicate a strong potential for subsurface target classification useful for dealing with false positives in buried landmine detection problems. Future work will focus on extending this work beyond these limiting assumptions.

References

[1] M. G. Fernández et al., "Synthetic aperture radar imaging system for landmine detection using a ground penetrating radar on board a unmanned aerial vehicle," *IEEE Access*, vol. 6, pp. 45100–45112, 2018.

[2] M. Garcia-Fernandez, A. Morgenthaler, Y. Alvarez-Lopez, F. Las Heras, and C. Rappaport, "Bistatic landmine and IED detection combining vehicle and drone mounted GPR sensors," *Remote Sens.*, vol. 11, no. 19, p. 2299, Oct. 2019.

[3] A. Ishimaru, *Wave Propagation and Scattering in Random Media*. New York, NY, USA: IEEE, 1997.

[4] A. D. Kim and C. Tsogka, "Synthetic aperture imaging of dispersive targets," *IEEE Trans. Comput. Imag.*, vol. 9, pp. 954–962, 2023.

[5] M. Masoodi, G. Esposito, G. Gennarelli, M. A. Maisto, F. Soldovieri, and R. Solimene, "Transverse resolution in 2-D linear inverse scattering by a multimonostatic/multifrequency configuration," *IEEE Geosci. Remote Sens. Lett.*, vol. 21, pp. 1–5, 2024.

[6] A. D. Kim and C. Tsogka, "Synthetic aperture radar imaging below a random rough surface," *Radio Sci.*, vol. 58, no. 12, p. 2023, Dec. 2023.

[7] D. J. Daniels, "A review of GPR for landmine detection," *Sens. Imag., Int. J.*, vol. 7, no. 3, pp. 90–123, Sep. 2006.

[8] L. Tsang, J. A. Kong, K.-H. Ding, and C. O. Ao, *Scattering of Electromagnetic Waves: Numerical Simulations*. Hoboken, NJ, USA: Wiley, 2004.

[9] A. D. Kim and C. Tsogka, "Modeling measurements for quantitative imaging subsurface targets," 2024.